ADVANCED MATERIALS
www.advmat.de

# Room-Temperature Out-Of-Plane Ferroelectricity in 1T′/1H $MoS_2$ Heterophase Bilayer

*Weijia Mu, Changming Ke, Changan Huangfu, Junhao Dong, Yaming Zhou,* Jingying Zheng, Shufang Yue, Jing Li, Shi Liu,* and Liying Jiao**

**The emergence of heterophase 2D materials, distinguished by their unique structures, has led to the discovery of a multitude of intriguing physical properties and a broad range of potential applications. Here, out-of-plane ferroelectricity is uncovered in a heterophase structure of 1T′/1H $MoS_2$, which is synthesized via chemical vapor deposition (CVD) by tuning the formation energies for $MoS_2$ with varied phases. The atomically resolved structures of the obtained 1T′/1H $MoS_2$ bilayers are captured using scanning transmission electron microscopy (STEM) and are confirmed to be non-centrosymmetric using second-harmonic generation (SHG) characterizations. The intrinsic out-of-plane polarization is visualized by piezoresponse force microscopy (PFM), which reveals that ferroelectric domains can be manipulated under an applied electric field. Ferroelectric tunnel junction (FTJ) devices fabricated on these bilayers exhibit reversible switching between a high resistance state (HRS) and a low resistance state (LRS). Density functional theory (DFT) calculations elucidate that the intrinsic ferroelectricity in 1T′/1H bilayers is attributed to interlayer sliding and lattice mismatch. The findings not only expand the scope of 2D ferroelectrics to include vertically stacked heterophase bilayers but also open avenues for exploring the coupling effect between ferroelectricity and other phenomena such as magnetism, superconductivity, and photocatalysis in 2D heterophase TMDCs.**

## 1. Introduction

The crystal phase plays a prominent role in determining the characteristics of low-dimensional materials, especially for 2D transition metal dichalcogenides (2D TMDCs).[1–5] For instance, $MoS_2$ possesses polymorphic structures like hexagonal (2H), rhombohedral (3R), and octahedral (1T) phases, as well as distorted octahedral phases (1T′, 1T′′, 1T′′′), which exhibits phase-dependent bandgaps and electronic properties.[6–10] The construction of heterophase structures from 2D TMDC layers with different phases has led to the emergence of many intriguing physical phenomena, including the introduction of ferromagnetism, enhancement of spin splitting, reduction of Schottky barriers, and facilitation of effective charge separation, among others.[11–16] These advances have paved the way for new applications of 2D heterophase structures across various fields, including spintronics, valleytronics, field-effect transistors, photocatalysis, and more.[17–22]

Beyond these newly discovered properties in 2D heterophase structures, the emerging concept of sliding ferroelectricity also holds promise for exploring potential ferroelectric properties in vertical heterophase structures of TMDCs. Wu et al. proposed an unconventional mechanism known as sliding ferroelectricity, predicting that specific stacking sequences of atomic layers in van der Waals (vdW) materials can facilitate interlayer charge transfer, leading to out-of-plane spontaneous polarization.[23] Unlike traditional ferroelectricity, which usually arises from the ions displacement within the unit cell and requires a non-centrosymmetric atomic structure, the concept of sliding ferroelectricity broadens the range of 2D ferroelectrics through feasible vdW stacking. Recently, this concept has been experimentally confirmed in bilayer or few layer TMDCs with specific stacking configurations, such as $WTe_2$,[24,25] bilayer h-BN,[26,27] 3R-stacked $MoS_2$ or $WSe_2$[28–33] and in heterostructures like $WS_2/MoS_2$ and graphene/h-BN.[34,35] However, heterophase structures, which consist of different phases of the same material, have not yet been reported to achieve sliding ferroelectricity.

Herein, we report experimental observation of ferroelectricity in a heterophase bilayer of 1T′/1H $MoS_2$ grown by chemical vapor deposition (CVD). Scanning transmission electron microscopy (STEM) and second-harmonic generation (SHG) characterizations were performed to identify the atomically resolved

---

W. Mu, C. Huangfu, Y. Zhou, S. Yue, L. Jiao
Key Laboratory of Organic Optoelectronics and Molecular Engineering of the Ministry of Education
Department of Chemistry
Tsinghua University
Beijing 100084, China
E-mail: ymzhou@mail.tsinghua.edu.cn; lyjiao@mail.tsinghua.edu.cn
C. Ke, S. Liu
Department of Physics
School of Science and Research Center for Industries of the Future
Westlake University
Hangzhou, Zhejiang 310030, China
E-mail: liushi@westlake.edu.cn
J. Dong, J. Zheng
College of Materials Science and Engineering
Fuzhou University
Fuzhou 350108, China
J. Li
Key Laboratory of Photochemical Conversion and Optoelectronic Materials
Technical Institute of Physics and Chemistry
Chinese Academy of Sciences
Beijing 100190, China

The ORCID identification number(s) for the author(s) of this article can be found under https://doi.org/10.1002/adma.202504941

**DOI: 10.1002/adma.202504941**

structures within the heterophase bilayer and to confirm its noncentrosymmetric nature. The intrinsic out-of-plane polarization at room temperature was confirmed by the 180° switchable ferroelectric domains by applying an external electric field, as evidenced by piezoresponse force microscopy (PFM). Additionally, we fabricated ferroelectric tunnel junction (FTJ) devices on 1T′/1H $MoS_2$ bilayers with both 0 and 180° stacking angles, and all the obtained FTJ devices displayed switchable tunneling resistance between two distinct stable states over $10^5$ cycles. We also revealed the distinct origin of the ferroelectricity in the 1T′/1H $MoS_2$ bilayers as a result of the interplay between interlayer sliding and strain induced by the lattice mismatch within the heterophase structure through theoretical calculations. The discovery of ferroelectricity in the 1T′/1H $MoS_2$ heterophase junction not only adds new members of 2D ferroelectrics but also provides a unique experimental platform for studying the relationship between ferroelectricity and the dimensions, structure, and electronic properties of materials, which helps to deepen our understanding of ferroelectric phenomena.

## 2. Results and Discussion

The key to exploring ferroelectricity in the 1T′/1H $MoS_2$ heterophase structure lies in the fabrication of heterophase bilayers with a clean interface. Compared to sequential stacking through controlled transfer, the direct growth of heterophase bilayers offers the most pristine interface, which is highly desirable for further investigation of their intrinsic properties. In our previous studies, we achieved one-step growth of 1T′/1H $MoS_2$ heterophase bilayers by using $K_2MoS_4$ as precursors.[36] This was accomplished by tuning the formation energy of the 1H and 1T′ phases of $MoS_2$ through excluding or introducing $K^+$ in the growth products by switching the atmosphere from inert Ar to reductive $H_2$/Ar. By carefully tuning the concentration of $H_2$ and the growth temperature (Figures S2 and S3, Supporting Information), we obtained 1T′/1H $MoS_2$ heterophase bilayers with a large area 1H bottom layer (up to 600 µm) and relatively small top 1T′ layers in a triangular shape (side length of ≈20 µm) on a fluorophlogopite mica substrate (**Figure** 1a,b) under the optimized growth conditions of 810 °C and an $H_2$/Ar ratio of 8:92 (Figure S1, Supporting Information, additional details are provided in the Experimental section). Most of the top 1T′ layers were aligned along the 0 and 180° directions relative to the bottom 1H layer, possibly because these two orientations are thermodynamically most stable.[37]

The bilayer nature of the obtained sample was confirmed by atomic force microscopy (AFM) measurements (Figure 1c; Figure S5, Supporting Information). To assess the phase purity and structural integrity of the obtained bilayers, we performed Raman spectroscopy, photoluminescence (PL), and STEM analysis. In a typical 0°-stacked heterophase bilayer (Figure 1c), the Raman spectrum of the single-layer region exhibited characteristic peaks at 384 $cm^{-1}$ ($E^1_{2g}$) and 402 $cm^{-1}$ ($A_{1g}$), with a peak separation of 18 $cm^{-1}$, consistent with the Raman spectral characteristics of single-layer 1H $MoS_2$.[38] In the bilayer region, the characteristic peaks of 1H $MoS_2$ shifted, with a separation of 22 $cm^{-1}$, indicating strong interlayer coupling.[39] Additional peaks were observed at 152 $cm^{-1}$ ($A_2$), 283 $cm^{-1}$, and 327 $cm^{-1}$ ($A_1$), which align with the Raman spectral features of 1T′ $MoS_2$ (Figure S4, Supporting Information).[40] The PL spectrum of the single-layer region presented a prominent fluorescence peak at 680 nm (1.82 eV) (Figure 1d), consistent with the optical bandgap of single-layer 1H $MoS_2$.[41] In contrast, the PL spectrum of the bilayer region lacked a distinct fluorescence peak, likely due to charge transfer between 1H and 1T′ layers, resulting in a reduced number of radiative recombination events.[42,43] Similar Raman and PL features were observed on 180°-stacked heterophase bilayers (Figure S6, Supporting Information). High-angle annular dark-field (HAADF)-STEM characterization was subsequently performed to visualize the atomic-scale structure at the boundary between 1T′/1H $MoS_2$ and 1H $MoS_2$ (Figure 1e; Figure S7, Supporting Information). In the 1H $MoS_2$ region, Mo and S atoms were regularly arranged at the lattice sites, whereas moiré superlattices were observed in the 1T′/1H $MoS_2$ region owing to lattice mismatch between the 1T′ and 1H phase. The selected area electron diffraction (SAED) patterns revealed hexagon and rectangle patterns, indicating the crystal symmetry corresponding to the diffracted spots of the 1H and 1T′ phases, respectively (Figure 1f).

Next, we measured the high-quality 1T′/1H $MoS_2$ bilayers with SHG. It is widely recognized that the single-layer 1H $MoS_2$ is a typical non-centrosymmetric 2D crystal that exhibits a strong SHG signal but lacks ferroelectricity.[44] The SHG spectra for both 1H $MoS_2$ and the 1T′/1H $MoS_2$ bilayers, in their respective orientations, displayed a six-petal symmetric pattern with a consistent polarization direction (**Figure** 2c,f), suggesting that there was no angular distortion between the top 1T′ $MoS_2$ layer and the bottom 1H $MoS_2$ layer.[45,46] Non-uniform SHG signals were observed particularly at 15 and 195°, which may stem from the strain effects at the interfaces.[47] The SHG mapping image collected on typical 1T′/1H $MoS_2$ bilayers with two stacking orientations showed varied intensities (Figure 2a). Notably, the SHG intensity in the 0°-stacked bilayer region was significantly higher than that of the 1H $MoS_2$, indicating an enhanced nonlinear optical response introduced by the stacking of 1T′ $MoS_2$. Conversely, the SHG polarization intensity in the 180°-stacked region was lower than that of 1H $MoS_2$, due to destructive interference between the SHG signals from the two parallel layers (Figure 2b,f).[48] Consequently, the 0°-stacked bilayer exhibits a stronger SHG response, indicating its potential for enhanced nonlinear optical properties and possible ferroelectric performance.

PFM measurements were then employed to investigate the boundary between the 1T′/1H $MoS_2$ and 1H $MoS_2$ regions transferred on conductive substrate (Figure S8, Supporting Information). PFM measurements on a 0°-stacked sample were performed by applying positive and negative bias to the designated areas (Figure 2d,e). The morphology of these biased region remained unchanged (Figure S12, Supporting Information), indicating that no electrochemical oxidation occurred under the PFM tip bias.[49] Phase and amplitude images revealed significant changes exclusively in the 1T′/1H stacked region upon the application of ±8 V while the 1H $MoS_2$ region remained unchanged. The 1T′/1H stacked region exhibited a typical butterfly-shaped amplitude curve and a hysteresis phase shift, indicative of a 180° ferroelectric domain flip (Figure 2h). In contrast, in the 1H region, the phase and amplitude curves overlapped in the hysteresis loop (Figure S9, Supporting Information).

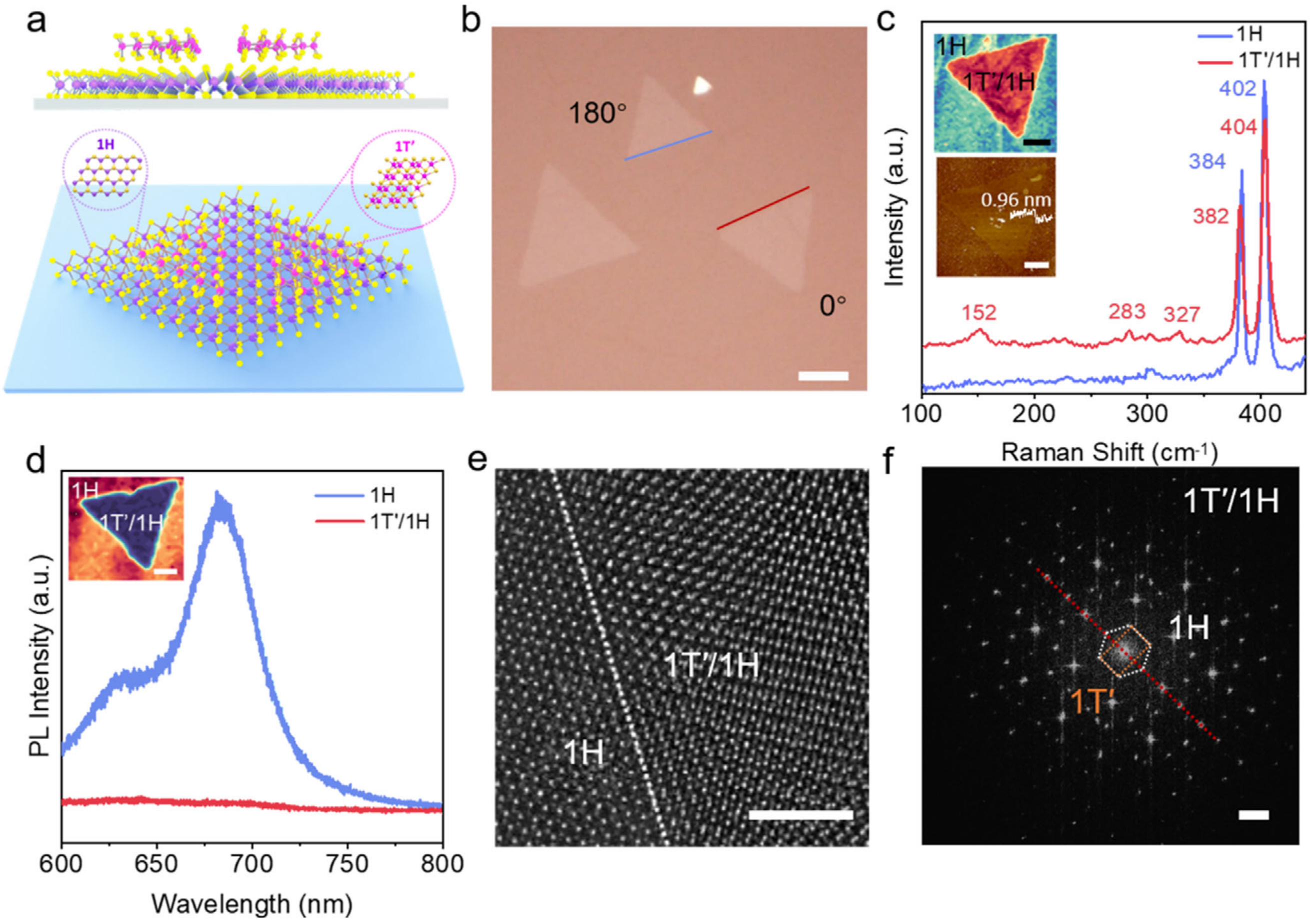

**Figure 1.** Characterizations of CVD-grown 1T′/1H $MoS_2$ heterophase bilayer. a) A schematic illustration of the 1T′/1H $MoS_2$ heterophase bilayer. Purple/magenta and yellow balls represent Mo and S atoms, respectively. b) A typical optical image of 1T′/1H $MoS_2$ heterophase bilayers on fluorophlogopite mica substrate, scale bar: 10 µm. The 1T′ $MoS_2$ triangles marked by blue and red lines, indicating orientations of 180 and 0° relative to the underlying 1H $MoS_2$ layer, respectively. c) Typical Raman spectra collected on the 1T′/1H $MoS_2$ heterophase bilayer region and 1H $MoS_2$ region. Insets, corresponding Raman mapping, and AFM images of a 1T′/1H $MoS_2$ heterophase bilayer, surrounded by 1H $MoS_2$, scale bars: 5 µm. d) Typical PL spectra of the 1T′/1H $MoS_2$ heterophase bilayer region and 1H $MoS_2$ region. Inset, corresponding PL mapping of the same sample shown in c), scale bar: 5 µm. e) A representative HAADF-STEM image captured at the 1T′/1H $MoS_2$-1H $MoS_2$ boundary, scale bar: 1 nm. f) SAED patterns of the 1T′/1H $MoS_2$ heterophase bilayer obtained through fast Fourier transform (FFT) analysis of the STEM image, scale bar: 5 1/nm. The dotted hexagon and rectangle denoted the crystal symmetry formed by diffracted spots of 1H and 1T′ regions, respectively.

Additional PFM measurements were performed on the monolayer 1T′ $MoS_2$. After applying ±8 V through the tip, no observable change in amplitude or phase was detected (Figure S10, Supporting Information). Collectively, these findings confirmed that the 1T′/1H stacking induced ferroelectric domain switching at the heterophase junction under an external electric field. Additionally, PFM analysis was extended to samples with 180° stacking orientation (Figure S11, Supporting Information). After PFM domain writing with positive and negative biases, the phase and amplitude of the 180°-stacked sample exhibited a less pronounced reversal compared to the 0°-stacked sample. This indicated that 1T′/1H $MoS_2$ samples with different orientations exhibited ferroelectricity, with the 0°-stacked sample showing a more pronounced effect. To exclude potential artifacts in PFM testing due to surface charges or static electricity from the applied biases,[50] the evolution of polarized domain patterns over time was examined (Figure 2g; Figure S12, Supporting Information). These observations substantiated the reliability of the PFM testing and further confirmed the out-of-plane ferroelectricity in 1T′/1H $MoS_2$.

The PFM analysis has proved the switchable ferroelectric polarization in 1T′/1H $MoS_2$, highlighting its potential application in miniaturized non-volatile memory devices. Therefore, we have fabricated FTJ devices by sandwiching 0°-stacked 1T′/1H $MoS_2$ heterophase bilayers between a monolayer graphene bottom electrode and a Cr/Au top electrode (**Figure 3**a; Figure S13, Supporting Information). An obvious counterclockwise hysteresis loop was observed as the DC bias changed (Figure 3b). Upon reaching a DC bias of +3.4 V, which corresponds to the coercive field of 1T′/1H $MoS_2$, the current underwent an abrupt transition from 27 to 95 µA, indicating a shift from the high resistance state (HRS) to the low resistance state (LRS) due to the change in the polarization-modulated tunneling barrier height. Conversely, when the DC bias fell below the negative coercive field of 1T′/1H

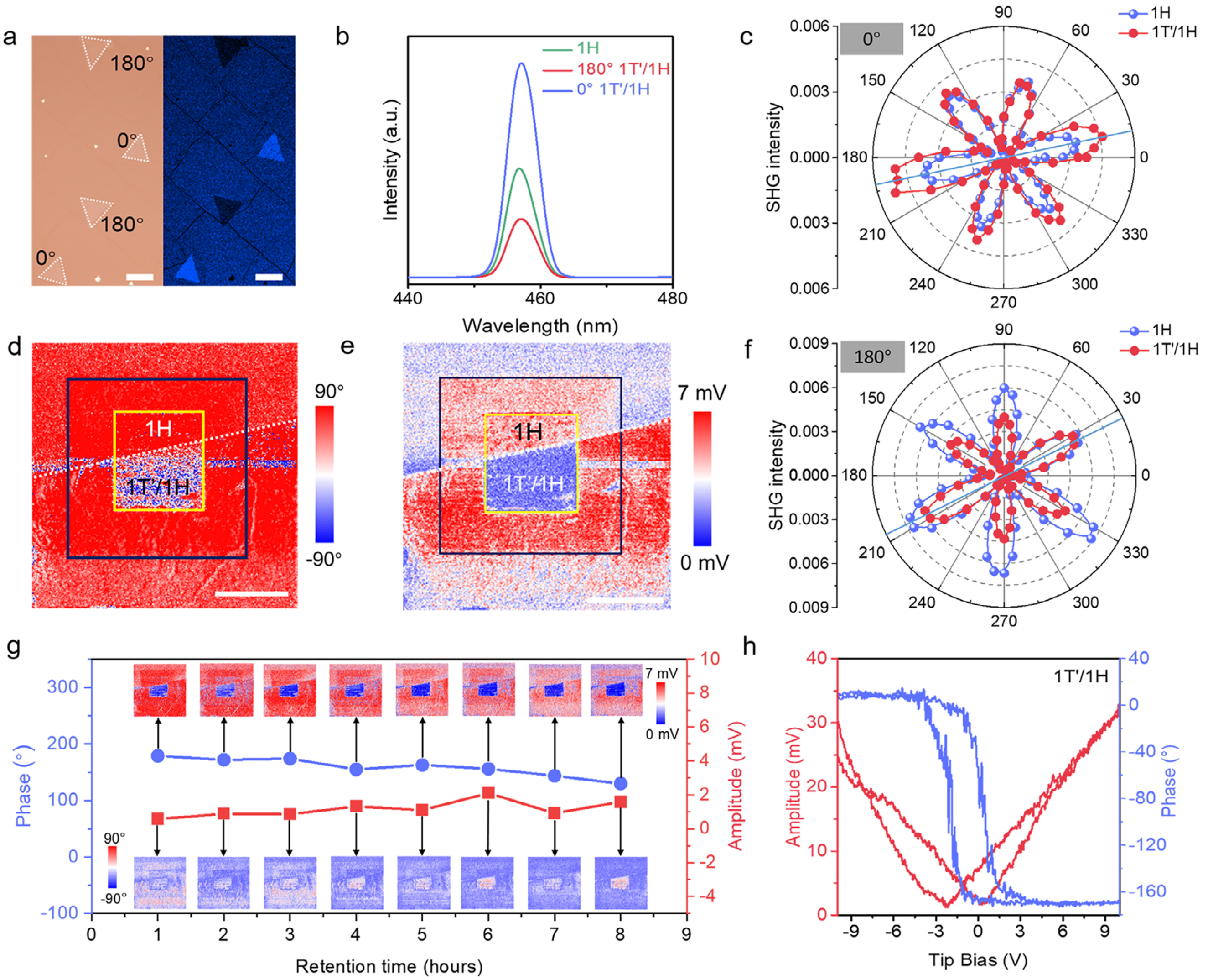

**Figure 2.** SHG characterization and piezoelectric response in 1T′/1H $MoS_2$ heterophase bilayer. a) Optical image of 1T′/1H $MoS_2$ heterophase bilayers (left) and the corresponding SHG intensity mapping image (right) surrounded by 1H $MoS_2$, scale bars: 20 µm. b) SHG spectra of 1T′/1H $MoS_2$ heterophase bilayers with two distinct stacking orientations and 1H $MoS_2$. c,f) Angle-dependent SHG intensity for 0 and 180° stacked 1T′/1H $MoS_2$ heterophase bilayers. d,e) PFM amplitude and OOP phase images of the 1T′/1H $MoS_2$ heterophase bilayer with surrounding 1H $MoS_2$ after electrical poling. The yellow and black box-in-box patterns were written by applying −8 and +8 V poling voltages, respectively. The dashed white line marks the boundary between 1T′/1H $MoS_2$ and 1H $MoS_2$ regions. Scale bars:1 µm. g) The retention of PFM amplitude and phase over time. The scanning areas for all images are 3.5 µm × 3.5 µm. h) Vertical PFM phase and amplitude hysteresis loops of 1T′/1H $MoS_2$ heterophase bilayer versus tip bias.

$MoS_2$ (−3.7 V), a switch from LRS to HRS was recorded, accompanied by a sudden change in current owing to ferroelectric effect. After being poled with a voltage of ± 4 V, higher than the coercive field, for 10 seconds, the FTJ device exhibited two distinct current values (11.9 and 25.7 µA) at a measuring voltage of 0.1 V, corresponding to HRS and LRS, respectively (Figure 3d). The retention property of the 1T′/1H $MoS_2$ showed that the two resistance states could be sustained for at least $10^4$ s (Figure 3e), implying a stable ferroelectric memory behavior. Raman spectroscopic measurements on the 1T′/1H $MoS_2$ bilayers, following the fabrication and characterization of the FTJ, confirmed that high phase stability of the 1T′ phase within the heterostructure (Figure S14, Supporting Information). To further verify that the observed electrical characteristics were due to the ferroelectricity of 1T′/1H $MoS_2$ instead of interface-induced hysteresis, the heterophase $MoS_2$ was transformed into pure 2H $MoS_2$ through an annealing process at 260 °C, followed by electrical testing using the same method. The Raman mapping image indicated that top 1T′ $MoS_2$ region has undergone a T′-H phase transition after annealing (Figure 3c). The current of the annealed FTJ exhibited a consistent curve over voltage change process, with no sudden changes in current. After being poled at ±4 V, the annealed FTJ displayed identical currents (1.1 µA at 0.1 V) over $10^3$ s, showing no obvious HRS or LRS (Figure S15, Supporting Information). In addition, FTJ devices based on 180°-stacked samples also displayed similar ferroelectric behavior (Figure S16, Supporting Information). To rule out ferroelectricity originating from individual phases, we fabricated FTJ devices using monolayer 1H

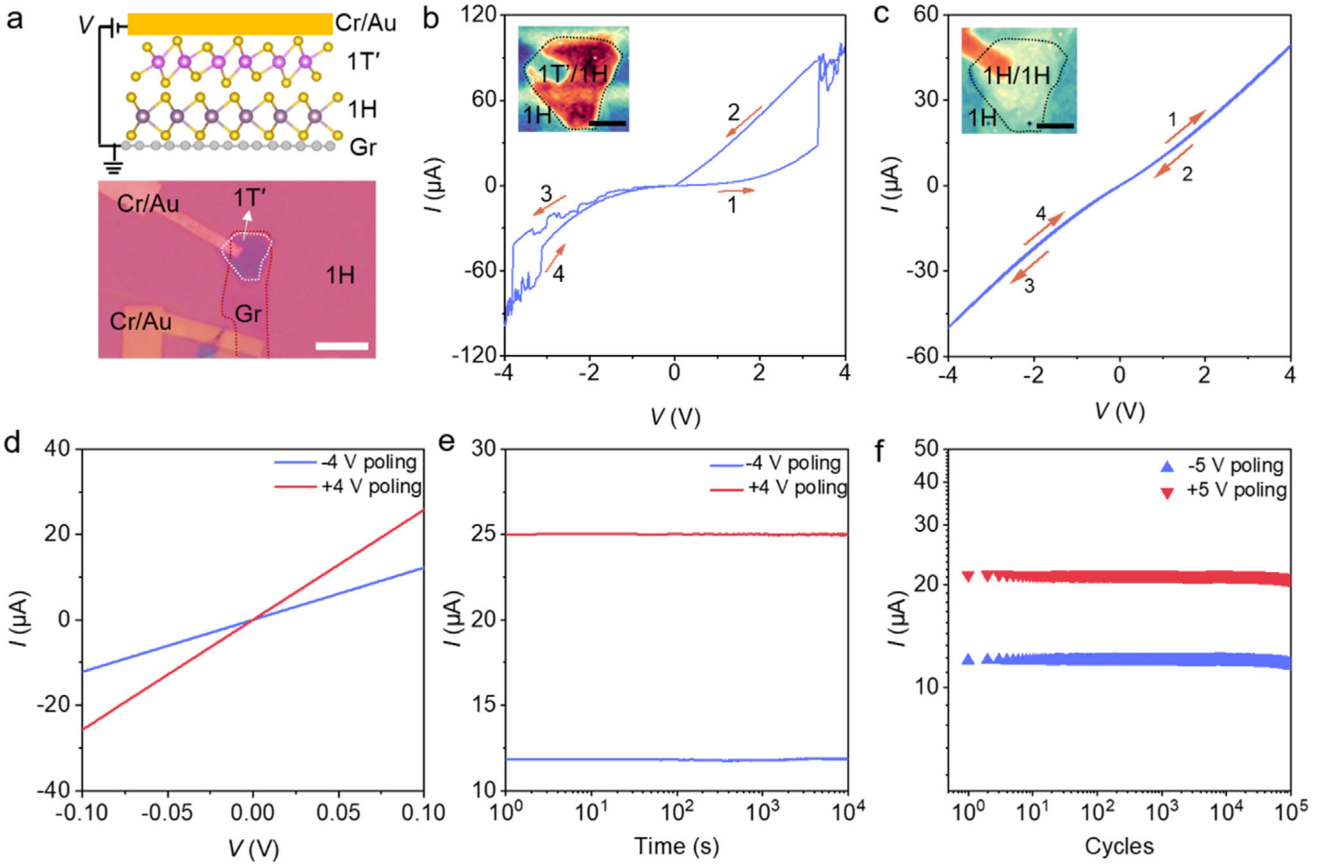

**Figure 3.** Tunneling current characterization of the FTJ device. a) Schematic illustration of FTJ based on 1T′/1H $MoS_2$ heterophase bilayer and the corresponding optical image, where the red and white dotted lines delineate the bottom graphene electrode and the 1T′ $MoS_2$, respectively. Scale bar: 10 µm. b) *I*–*V* characteristics of the FTJ device demonstrate tunneling electroresistance between the LRS and HRS states. The arrows indicate the direction of the current change. Inset: A Raman mapping image of the measured FTJ device, scale bar: 5 µm. c) *I*–*V* characteristics of same device after annealing at 260 °C, exhibiting no difference in tunneling electroresistance with respect to the poling voltage. Inset: A Raman mapping image of the device after annealing, displaying the complete conversion of T′ phase to H phase, scale bar: 5 µm. d) The polarization-dependent tunneling current versus the applied DC field through the FTJ device. The tunneling current is strongly dependent on the previous poling voltage. e) Retention properties of the bistate after applying +4 and −4 V poling voltages. f) Fatigue analysis of another FTJ over $10^5$ switching cycles.

$MoS_2$ and 1T′ $MoS_2$ as functional layers, respectively. Neither configuration exhibited ferroelectric switching or hysteretic resistive states (Figure S17, Supporting Information). These results further confirmed that 1T′/1H $MoS_2$ heterophase bilayer exhibited intrinsic ferroelectricity, which is consistent with the PFM results. To further evaluate the fatigue resistance of the 1T′/1H $MoS_2$ bilayer, periodic bipolar voltage pulses were applied to repeatedly reverse the polarization direction of another FTJ device (Figure S18, Supporting Information). Over $10^5$ switching cycles, the FTJ maintained a stable HRS current (≈12.1 µA) and LRS current (≈21.0 µA) at a readout voltage of 1.0 V, exhibiting negligible fatigue and no wake-up effect, showing high fatigue resistance (Figure 3f).

To uncover the underlying mechanisms of 2D ferroelectricity, we conducted density functional theory (DFT) calculations on the 1T′/1H junction. Our theoretical findings indicate that the intrinsic out-of-plane ferroelectricity of this heterophase junction results from interlayer sliding and strain generated by lattice mismatch. Initially, the Mo atoms in the 1T′ phase align with the S-site of the 1H phase (AA-down), corresponding to a negative polarization state. As the 1T′ phase slides relative to the 1H phase, the structural configuration transitions through intermediate states 2-3-4 and eventually reaches structure 5, in which the Mo atoms in the 1H phase are positioned near the S atoms of 1T′ phase (AA-up), leading to a polarization reversal from negative to positive (**Figure** 4a). Under the influence of strain caused by lattice mismatch, the polarization vector switches from −0.30 to +0.58 pC $m^{-1}$ (Figure S19, Supporting Information). The sliding from the AA-down configuration to the AA-up configuration requires overcoming an energy barrier of 5.3 meV per formula unit (Figure 4b; Figure S20, Supporting Information), which is comparable to that of typical sliding ferroelectrics such as bilayer h-BN.[27] This sliding ferroelectric mechanism, which minimizes ionic displacement and charge trapping at interfaces,[33] contributes to the high fatigue resistance in the heterophase bilayer. The interfacial differential charge densities (DCD) clearly show the interlayer charge transfer between the top and bottom layers of the heterophase bilayers, as evidenced by the distinct separation of electron accumulation and electron depletion regions (Figure 4c,d). Consequently, we propose that the

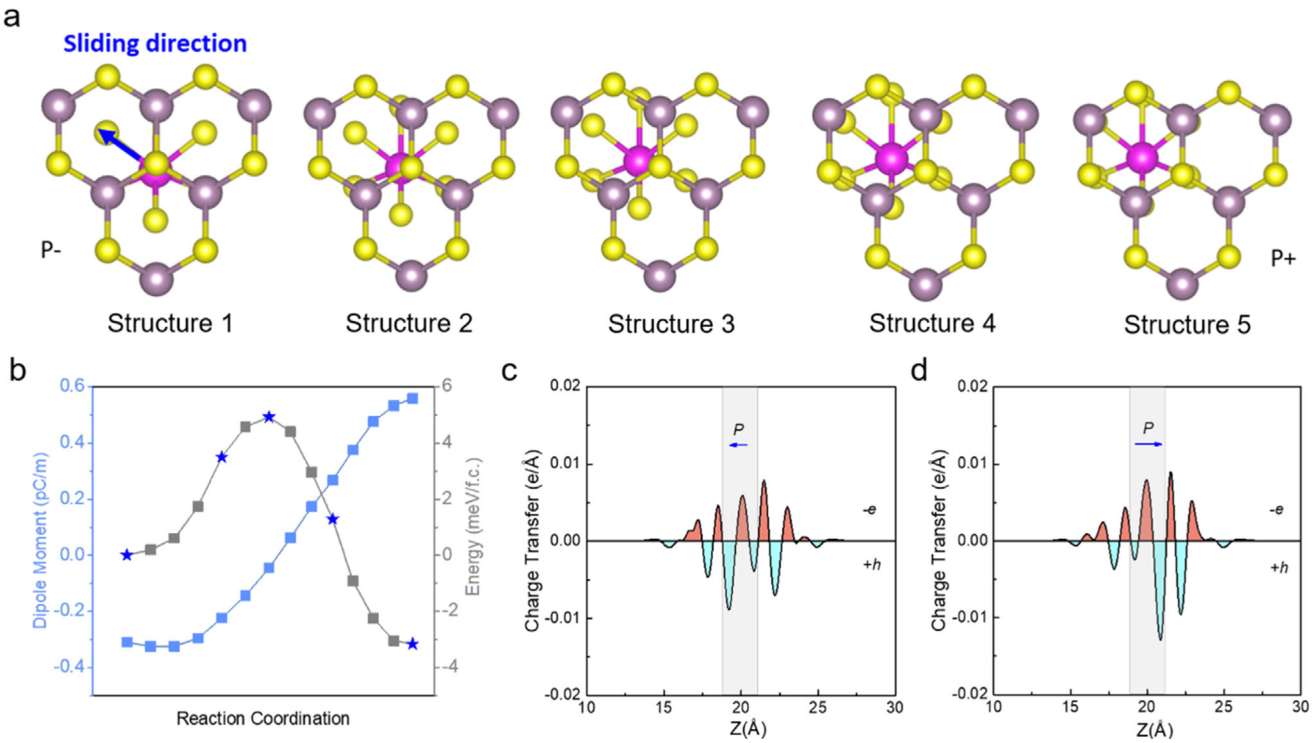

**Figure 4.** Ferroelectric behavior of the 1T′/1H $MoS_2$ heterophase bilayer enabled by interlayer sliding. a) Top view of the initial stacking order (AA-down, structure 1) where a top-layer S atom is positioned directly above an interfacial Mo atom of the bottom layer. The purple, magenta, and yellow spheres represent the top Mo, bottom Mo, and S atoms, respectively. Lateral sliding of the top layer along the armchair direction leads to a new stacking order (AA-up, structure 5), in which the top-layer Mo atom is now positioned adjacent to and below the interfacial S atom of the bottom layer. Structures 2–4 represent intermediate configurations in the sliding process. b) The spontaneous OOP polarization value and relative energy vary as a function of the reaction coordination. c,d) The interlayer differential charge density for the up (AA-up) and down (AA-down) polarization states, respectively.

ferroelectricity of 1T′/1H heterophase junction is closely related to interlayer sliding and also correlated with the lattice mismatch between the different crystal phases.

## 3. Conclusion

In summary, we have devised a new 2D ferroelectric material in the form of a 1T′/1H $MoS_2$ heterophase bilayer and elucidated its sliding ferroelectricity mechanism through a combination of experimental and theoretical approaches. The key of this research lies in the fabrication of heterophase bilayers with a pristine and intrinsic interface, thereby enhancing the interlayer coupling. This was achieved by direct growth using $K_2MoS_4$ as a precursor and adjusting the formation energy of the 1H and 1T′ phases by altering the growth atmosphere. Comprehensive analyses, including Raman spectroscopy, photoluminescence, and STEM, verified the phase purity and structural integrity of the bilayers. SHG measurements confirmed the noncentrosymmetric nature of the 1T′/1H bilayer, and PFM measurements established the presence of out-of-plane ferroelectricity in the heterophase bilayer with different stacking orientations. The fabrication of FTJ devices and the observation of polarization-dependent tunneling currents underscored the potential of 1T′/1H heterophase bilayer for non-volatile memory applications. DFT calculations revealed that the intrinsic ferroelectricity of the 1T′/1H junction arises from interlayer sliding and strain formed by lattice mismatch, resulting in an out-of-plane polarization vector. Given previous reports of superconductivity in 1T′ $MoS_2$[6,51] and magnetism in 1T′/1H $MoS_2$,[52] the discovery of ferroelectricity positions 1T′/1H $MoS_2$ as an ideal platform for investigating the interplay between ferroelectricity, superconductivity, and magnetism, potentially leading to novel physical phenomena. Furthermore, the electric field tunable tunneling at the 1T′/1H $MoS_2$ interface holds promise for enhancing the functionality of all-2D field effect transistors, with 1T′/1H $MoS_2$ serving as contacts and 1H $MoS_2$ as the semiconducting channel. Our findings are expected to stimulate the development of other bilayer or multilayer ferroelectric TMDCs based on heterophase structures, fostering both the exploration of new physics and the creation of new devices with integrated logic and memory functions.

## 4. Experimental Section

*Preparation of 2D 1T′/1H $MoS_2$ Heterophase Bilayer*: The precursor $K_2MoS_4$ was prepared according to the previously reported synthesis procedures.[36] $K_2MoS_4$ (≈10 mg) was placed on top of a piece of fluorophlogopite mica in a tube furnace. Another piece of fluorophlogopite mica, serving as the growth substrate, was positioned under the precursor. The system was heated up to 810 °C in a pure Ar atmosphere (100 sccm) over a period of 40 min. Upon reaching the growth temperature, the furnace was held at this temperature for an additional 10 min to facilitate the growth of bottom 1H layer. Subsequently, the atmosphere was switched to a mixture of 8 sccm $H_2$/92 sccm Ar gas, and this was maintained for 3 min to allow for the growth of the top 1T′ layer. Finally, the tube furnace was rapidly cooled down to room temperature. The synthesis was conducted in a 1-inch quartz tube (Figure S1, Supporting Information).

*Microscopic and Spectroscopic Characterizations*: Optical images were captured using a BX 51 M microscope (Olympus). Raman spectroscopic measurements were conducted with a HORIBA-Jobin-Yvon system, utilizing a 532 nm laser at 1 mW power. AFM measurements were performed with a Dimension Icon instrument (Bruker) in tapping mode. The HAADF-STEM images were obtained using an aberration-corrected JEM-ARM300F operated at 300 kV.

*SHG Measurements*: Optical SHG signals were collected using a convert confocal microscope (Nikon, A1) with a femtosecond laser source (Coherent Co., Chameleon, a pulse width of 140 fs, a repetition rate of 80 MHz, output wavelength range of 700–1060 nm). The laser was modulated by a laser power attenuation. After adjusting the attenuation plate to regulate the laser power and the Galvano scanner, the beam entered into the microscope and was focused onto a spot with an objective lens (40×, NA 0.95). The signal generated by the sample was collected through the same microscope objective, transmitted through a low-pass filter, and then entered into the spectral detector unit with 32 channels. The wavelength detection range was 400 – 650 nm, with a wavelength resolution of 2.5 nm. Angle-dependent SHG signals were collected using a Stanford SR830 DSP Lock-In Amplifier, which was coupled to a Light Conversion PHAROS femtosecond laser. The excitation source was ultrafast pulse light at ≈1030 nm. A 20× objective lens was used to focus the laser, producing a spot diameter of ≈5.5 µm. The sample was fixed while the polarization of the incident light was rotated in 6° increments to obtain spectra at various angles.

*PFM Measurements*: Ferroelectric polarization of the 1T′/1H $MoS_2$ heterophase bilayer was examined using a piezoresponse force microscope (Bruker Dimension Icon) at room temperature. Measurements were carried out in resonance-enhanced mode using conductive Pt/Ir tips with a spring constant of 3 N $m^{-1}$. The resonance frequency for OOP measurement was set at ≈300 kHz. PFM hysteresis loops were recorded by applying a tip bias of ±8 V to the samples.

*The Fabrication and Measurements of FTJ Devices*: A single layer of graphene flake was mechanically exfoliated onto a $SiO_2$/Si substrate. Following this, a 1T′/1H $MoS_2$ bilayer was placed on top of the graphene with the aid of poly (methyl methacrylate) (PMMA) and polydimethylsiloxane (PDMS) using a fixed-point transfer set-up. PDMS and PMMA were subsequently removed from the 1T′/1H $MoS_2$ bilayer by heating at 80 °C and soaking in a toluene, respectively. Finally, a 10 nm Cr/30 nm Au electrode was fabricated on the 1T′/1H $MoS_2$ bilayer using EBL, thermal evaporation, and lift-off, resulting in a ferroelectric tunnel junction device with 1T′/1H $MoS_2$ serving as the vertical channel, single-layer graphene and metal electrode as the bottom and top electrodes, respectively. The electrical transport properties were measured in a probe station equipped with a Keysight B1500A semiconductor analyzer in vacuum ($10^{-5}$ mbar) at room temperature. The fatigue analysis was measured in a probe station equipped with a Keysight B1530 semiconductor analyzer at room temperature.

*Theoretical Calculations*: DFT calculations were carried out using the Vienna Ab initio Simulation Package (VASP). The Perdew-Burke-Ernzerhof (PBE) functional was utilized for describing exchange-correlation interactions, combined with van der Waals corrections. The projector augmented wave (PAW) method was used to model the interaction between valence electrons and the core ion. An energy cutoff of 600 eV was set for the calculations. Geometry optimizations were performed with the conjugate gradient algorithm until forces were reduced to <0.01 V Å$^{-1}$. Electronic self-consistent calculations were converged to $10^{-7}$ eV. The Brillouin zone was sampled using a 7 × 5 × 1 *k*-point Monkhorst-Pack mesh for the unit cell. A vacuum region thicker than 15 Å was included in the structural model. A planar dipole correction was introduced into the middle of the vacuum region to compensate for electrostatic interactions between dipole layers, following the procedure implemented in VASP.

## Supporting Information

Supporting Information is available from the Wiley Online Library or from the author.

## Acknowledgements

W.M., C.K., and C.H. contributed equally to this work. L.J. acknowledges support from the Tsinghua-Toyota Joint Research Fund and the National Natural Science Foundation of China (Grant No. 21925504 and 22275111). S.L. acknowledges support from the National Natural Science Foundation of China (Grant No. 12304128) and the computational resources provided by Westlake HPC Center. Y.Z. acknowledges support from the National Natural Science Foundation of China (Grant No. 22105115).

## Conflict of Interest

The authors declare no conflict of interest.

## Data Availability Statement

The data that support the findings of this study are available from the corresponding author upon reasonable request.

## Keywords

2D, chemical vapor deposition, ferroelectricity, heterophase junction, phase engineering

Received: March 13, 2025
Revised: April 4, 2025

[1] Y. Chen, Z. Lai, X. Zhang, Z. Fan, Q. He, C. Tan, H. Zhang, *Nat. Rev. Chem.* **2020**, *4*, 243.
[2] D. Kim, J. Pandey, J. Jeong, W. Cho, S. Lee, S. Cho, H. Yang, *Chem. Rev.* **2023**, *123*, 11230.
[3] W. Li, X. Qian, J. Li, *Nat. Rev. Mater.* **2021**, *6*, 829.
[4] H. Liu, Y. Wu, Z. Wu, S. Liu, V. L. Zhang, T. Yu, *ACS Nano* **2024**, *18*, 2708.
[5] X. Yin, C. S. Tang, Y. Zheng, J. Gao, J. Wu, H. Zhang, M. Chhowalla, W. Chen, A. T. S. Wee, *Chem. Soc. Rev.* **2021**, *50*, 10087.
[6] Y. Fang, J. Pan, J. He, R. Luo, D. Wang, X. Che, K. Bu, W. Zhao, P. Liu, G. Mu, H. Zhang, T. Lin, F. Huang, *Angew. Chem., Int. Ed.* **2018**, *57*, 1232.
[7] S. Manzeli, D. Ovchinnikov, D. Pasquier, O. V. Yazyev, A. Kis, *Nat. Rev. Mater.* **2017**, *2*, 17033.
[8] J. Suh, T. L. Tan, W. Zhao, J. Park, D.-Y. Lin, T.-E. Park, J. Kim, C. Jin, N. Saigal, S. Ghosh, Z. M. Wong, Y. Chen, F. Wang, W. Walukiewicz, G. Eda, J. Wu, *Nat. Commun.* **2018**, *9*, 199.
[9] Q. H. Wang, K. Kalantar-Zadeh, A. Kis, J. N. Coleman, M. S. Strano, *Nat. Nanotechnol.* **2012**, *7*, 699.
[10] W. Zhao, J. Pan, Y. Fang, X. Che, D. Wang, K. Bu, F. Huang, *Chem.-Eur. J.* **2018**, *24*, 15942.
[11] S. Radhakrishnan, D. Das, L. Deng, P. M. Sudeep, G. Colas, C. A. de los Reyes, S. Yazdi, C. W. Chu, A. A. Martí, C. S. Tiwary, T. Filleter, A. K. Singh, P. M. Ajayan, *Adv. Mater.* **2018**, *30*, 1803366.
[12] V. Kochat, A. Apte, J. A. Hachtel, H. Kumazoe, A. Krishnamoorthy, S. Susarla, J. C. Idrobo, F. Shimojo, P. Vashishta, R. Kalia, A. Nakano, C. S. Tiwary, P. M. Ajayan, *Adv. Mater.* **2017**, *29*, 1703754.

[13] A. Ciarrocchi, F. Tagarelli, A. Avsar, A. Kis, *Nat. Rev. Mater.* **2022**, *7*, 449.
[14] Z. Fan, X. Jiang, J. Luo, L. Jiao, R. Huang, S. Li, L. Wang, *Phys. Rev. B* **2017**, *96*, 165402.
[15] X. Xu, S. Chen, S. Liu, X. Cheng, W. Xu, P. Li, Y. Wan, S. Yang, W. Gong, K. Yuan, P. Gao, Y. Ye, L. Dai, *J. Am. Chem. Soc.* **2019**, *141*, 2128.
[16] K. Chang, X. Hai, H. Pang, H. Zhang, L. Shi, G. Liu, H. Liu, G. Zhao, M. Li, J. Ye, *Adv. Mater.* **2016**, *28*, 10033.
[17] J. Choi, C. Lane, J.-X. Zhu, S. A. Crooker, *Nat. Mater.* **2022**, *22*, 305.
[18] H. Liu, D. Fu, X. Li, J. Han, X. Chen, X. Wu, B. Sun, W. Tang, C. Ke, Y. Wu, Z. Wu, J. Kang, *ACS Nano* **2021**, *15*, 8244.
[19] S. Cho, S. Kim, J. H. Kim, J. Zhao, J. Seok, D. H. Keum, J. Baik, D.-H. Choe, K. J. Chang, K. Suenaga, S. W. Kim, Y. H. Lee, H. Yang, *Science* **2015**, *349*, 625.
[20] R. Kappera, D. Voiry, S. E. Yalcin, B. Branch, G. Gupta, A. D. Mohite, M. Chhowalla, *Nat. Mater.* **2014**, *13*, 1128.
[21] J. H. Sung, H. Heo, S. Si, Y. H. Kim, H. R. Noh, K. Song, J. Kim, C.-S. Lee, S.-Y. Seo, D.-H. Kim, H. K. Kim, H. W. Yeom, T.-H. Kim, S.-Y. Choi, J. S. Kim, M.-H. Jo, *Nat. Nanotechnol.* **2017**, *12*, 1064.
[22] R. Peng, L. Liang, Z. D. Hood, A. Boulesbaa, A. Puretzky, A. V. Ievlev, J. Come, O. S. Ovchinnikova, H. Wang, C. Ma, M. Chi, B. G. Sumpter, Z. Wu, *ACS Catal.* **2016**, *6*, 6723.
[23] L. Li, M. Wu, *ACS Nano* **2017**, *11*, 6382.
[24] P. Sharma, F.-X. Xiang, D.-F. Shao, D. Zhang, E. Y. Tsymbal, A. R. Hamilton, J. Seidel, *Sci. Adv.* **2019**, *5*, 1603113.
[25] J. Xiao, Y. Wang, H. Wang, C. D. Pemmaraju, S. Wang, P. Muscher, E. J. Sie, C. M. Nyby, T. P. Devereaux, X. Qian, X. Zhang, A. M. Lindenberg, *Nat. Phys.* **2020**, *16*, 1028.
[26] K. Yasuda, X. Wang, K. Watanabe, T. Taniguchi, P. Jarillo-Herrero, *Science* **2021**, *372*, 1458.
[27] M. Vizner Stern, Y. Waschitz, W. Cao, I. Nevo, K. Watanabe, T. Taniguchi, E. Sela, M. Urbakh, O. Hod, M. Ben Shalom, *Science* **2021**, *372*, 1462.
[28] X. Wang, K. Yasuda, Y. Zhang, S. Liu, K. Watanabe, T. Taniguchi, J. Hone, L. Fu, P. Jarillo-Herrero, *Nat. Nanotechnol.* **2022**, *17*, 367.
[29] A. Weston, E. G. Castanon, V. Enaldiev, F. Ferreira, S. Bhattacharjee, S. Xu, H. Corte-Leon, Z. Wu, N. Clark, A. Summerfield, T. Hashimoto, Y. Gao, W. Wang, M. Hamer, H. Read, L. Fumagalli, A. V. Kretinin, S. J. Haigh, O. Kazakova, A. K. Geim, V. I. Fal'ko, R. Gorbachev, *Nat. Nanotechnol.* **2022**, *17*, 390.
[30] T. H. Yang, B.-W. Liang, H.-C. Hu, F.-X. Chen, S.-Z. Ho, W.-H. Chang, L. Yang, H.-C. Lo, T.-H. Kuo, J.-H. Chen, P.-Y. Lin, K. B. Simbulan, Z.-F. Luo, A. C. Chang, Y.-H. Kuo, Y.-S. Ku, Y.-C. Chen, Y.-J. Huang, Y.-C. Chang, Y.-F. Chiang, T.-H. Lu, M.-H. Lee, K.-S. Li, M. Wu, Y.-C. Chen, C.-L. Lin, Y.-W. Lan, *Nat. Electron.* **2023**, *7*, 29.
[31] H. Jiang, L. Li, Y. Wu, R. Duan, K. Yi, L. Wu, C. Zhu, L. Luo, M. Xu, L. Zheng, X. Gan, W. Zhao, X. Wang, Z. Liu, *Adv. Mater.* **2024**, *36*, 2400670.
[32] P. Meng, Y. Wu, R. Bian, E. Pan, B. Dong, X. Zhao, J. Chen, L. Wu, Y. Sun, Q. Fu, Q. Liu, D. Shi, Q. Zhang, Y. W. Zhang, Z. Liu, F. Liu, *Nat. Commun.* **2022**, *13*, 7696.
[33] R. Bian, R. He, E. Pan, Z. Li, G. Cao, P. Meng, J. Chen, Q. Liu, Z. Zhong, W. Li, F. Liu, *Science* **2024**, *385*, 57.
[34] L. Rogée, L. Wang, Y. Zhang, S. Cai, P. Wang, M. Chhowalla, W. Ji, S. P. Lau, *Science* **2022**, *376*, 973.
[35] R. Niu, Z. Li, X. Han, Z. Qu, D. Ding, Z. Wang, Q. Liu, T. Liu, C. Han, K. Watanabe, T. Taniguchi, M. Wu, Q. Ren, X. Wang, J. Hong, J. Mao, Z. Han, K. Liu, Z. Gan, J. Lu, *Nat. Commun.* **2022**, *13*, 6241.
[36] L. Liu, J. Wu, L. Wu, M. Ye, X. Liu, Q. Wang, S. Hou, P. Lu, L. Sun, J. Zheng, L. Xing, L. Gu, X. Jiang, L. Xie, L. Jiao, *Nat. Mater.* **2018**, *17*, 1108.
[37] J. Dong, L. Zhang, X. Dai, F. Ding, *Nat. Commun.* **2020**, *11*, 5862.
[38] C. Lee, H. Yan, L. E. Brus, T. F. Heinz, J. Hone, S. Ryu, *ACS Nano* **2010**, *4*, 2695.
[39] J. Zhang, J. Wang, P. Chen, Y. Sun, S. Wu, Z. Jia, X. Lu, H. Yu, W. Chen, J. Zhu, G. Xie, R. Yang, D. Shi, X. Xu, J. Xiang, K. Liu, G. Zhang, *Adv. Mater.* **2015**, *28*, 1950.
[40] Y. Yu, G.-H. Nam, Q. He, X.-J. Wu, K. Zhang, Z. Yang, J. Chen, Q. Ma, M. Zhao, Z. Liu, F.-R. Ran, X. Wang, H. Li, X. Huang, B. Li, Q. Xiong, Q. Zhang, Z. Liu, L. Gu, Y. Du, W. Huang, H. Zhang, *Nat. Chem.* **2018**, *10*, 638.
[41] K. F. Mak, C. Lee, J. Hone, J. Shan, T. F. Heinz, *Phys. Rev. Lett.* **2010**, *105*, 136805.
[42] Y. Gong, J. Lin, X. Wang, G. Shi, S. Lei, Z. Lin, X. Zou, G. Ye, R. Vajtai, B. I. Yakobson, H. Terrones, M. Terrones, B. K. Tay, J. Lou, S. T. Pantelides, Z. Liu, W. Zhou, P. M. Ajayan, *Nat. Mater.* **2014**, *13*, 1135.
[43] Y. Jiang, S. Chen, W. Zheng, B. Zheng, A. Pan, *Light: Sci. Appl.* **2021**, *10*, 72.
[44] N. Kumar, S. Najmaei, Q. Cui, F. Ceballos, P. M. Ajayan, J. Lou, H. Zhao, *Phys. Rev. B* **2013**, *87*, 161403.
[45] J. C. Arias-Muñoz, H. Kaaripuro, Y. Zhang, S. Das, H. A. Fernandez, Z. Sun, *Adv. Funct. Mater.* **2023**, *34*, 2310365.
[46] M. Xu, H. Ji, M. Zhang, L. Zheng, W. Li, L. Luo, M. Chen, Z. Liu, X. Gan, X. Wang, W. Huang, *Adv. Mater.* **2024**, 2313638.
[47] K. C. Chiu, K. H. Huang, C. A. Chen, Y. Y. Lai, X. Q. Zhang, E. C. Lin, M. H. Chuang, J. M. Wu, Y. H. Lee, *Adv. Mater.* **2017**, *30*, 1704796.
[48] W.-T. Hsu, Z.-A. Zhao, L.-J. Li, C.-H. Chen, M.-H. Chiu, P.-S. Chang, Y.-C. Chou, W.-H. Chang, *ACS Nano* **2014**, *8*, 2951.
[49] P. Zhao, R. Wang, D. H. Lien, Y. Zhao, H. Kim, J. Cho, G. H. Ahn, A. Javey, *Adv. Mater.* **2019**, *31*, 1900136.
[50] R. K. Vasudevan, N. Balke, P. Maksymovych, S. Jesse, S. V. Kalinin, *Appl. Phys. Rev.* **2017**, *4*, 021302.
[51] J. Peng, Y. Liu, X. Luo, J. Wu, Y. Lin, Y. Guo, J. Zhao, X. Wu, C. Wu, Y. Xie, *Adv. Mater.* **2019**, *31*, 1900568.
[52] L. Cai, J. He, Q. Liu, T. Yao, L. Chen, W. Yan, F. Hu, Y. Jiang, Y. Zhao, T. Hu, Z. Sun, S. Wei, *J. Am. Chem. Soc.* **2015**, *137*, 2622.